Strain Heterogeneity and Damage Nucleation at Grain Boundaries during Monotonic Deformation in Commercial Purity Titanium

T.R. Bieler, M.A. Crimp, Y. Yang, L. Wang, P. Eisenlohr, D.E. Mason, W. Liu, and G.E. Ice

Heterogeneous strain was analyzed in polycrystalline, commercial-purity titanium using many experimental techniques that provide information about microstructure, dislocation arrangement, grain orientation, orientation gradients, surface topography, and local strain gradients. The recrystallized microstructure with 50–200 μm grains was extensively characterized before and after deformation using 4-point bending to strains between 2% and 15%. Extremely heterogeneous deformation occurred along some grain boundaries, leading to orientation gradients exceeding 10° over 10–20 μm. Patches of highly characterized microstructure were modeled using crystal plasticity finite element (CPFE) analysis to simulate the deformation to evaluate the ability of the CPFE model to capture local deformation processes. Damage nucleation events were identified that are associated with twin interactions with grain boundaries. Progress toward identifying fracture initiation criteria based upon slip and twin interactions with grain boundaries is illustrated with related CPFE simulations of deformation in a TiAl alloy.

INTRODUCTION

It is commonly thought that damage nucleation occurs in regions of strain concentration, either macroscopically or microscopically. While finite element analysis is commonly used to identify regions of macroscopic strain concentration at the component level, such that changes in shape can improve a design, this approach is not as simple at the microstructural scale, where heterogeneous strain is typically observed in polycrystals. Heterogeneous strain results from the fact that some crystal orientations are softer than others. This phenomenon can be modeled effectively with visco-plastic self-consistent models to describe homogenized deformation behavior of a material, for example.[1,2] However, the constraint of one grain on deformation of a neighboring grain leads to heterogeneous deformation within a given grain,[3,4] which cannot be modeled effectively using homogenized statistical modeling approaches. Thus, crystal plasticity finite element (CPFE) analysis is needed to model the deformation processes that occur in three-dimensional (3-D) microstructures, where the interactive effects of grain shape and orientation-dependent slip processes can be modeled.[5–11] As damage nucleation is a rare event that occurs in particular geometrical grain arrangements, it is necessary to be able to predict these deformation processes accurately before damage nucleation sites can be predicted with any confidence. Consequently, research has focused on two important phenomena: detailed characterization and modeling of heterogeneous deformation, and identification of damage nucleation mechanisms that occur at grain or phase boundaries.

Prior work in identifying conditions for fracture or cavity nucleation in titanium-based alloys suggests that particular kinds of slip interactions with a grain boundary can weaken the boundary, or highly anisotropic plastic strains can cause triaxial stresses that favor cavity or crack nucleation.[12–14] In this research program, we are using commercial-purity titanium (CP Ti) as a model material to study how grains with different orientations deform, to identify particular grain boundary regions where heterogeneous deformation occurs, and to identify where heterogeneous deformation leads to damage nucleation events. Discoveries from this experimental work show that deformation near boundaries varies significantly, depending on grain orientations and shape. In some locations, sliding or mode II cracks and extreme rotation gradients within a few micrometers of the grain boundary have been observed, leading to dramatic topography along some grain boundaries, while other boundaries exhibit no topographic features.

To increase understanding of what kinds of heterogeneous deformation processes cause damage nucleation, CPFE modeling of patches of highly characterized microstructure is under

How would you…

…describe the overall significance of this paper?

Complex 3-D deformation processes at grain boundaries can be characterized using a combination of synergistic techniques.

…describe this work to a materials science and engineering professional with no experience in your technical specialty?

Prediction of damage nucleation at grain boundaries requires models that can accurately predict heterogeneous deformation, which requires accurate experimental characterization to assist model development and validation.

…describe this work to a layperson?

Quantitative understanding about what happens just before a crack becomes a crack will lead to new material processing and design paradigms that will improve material performance in a wide range of applications.

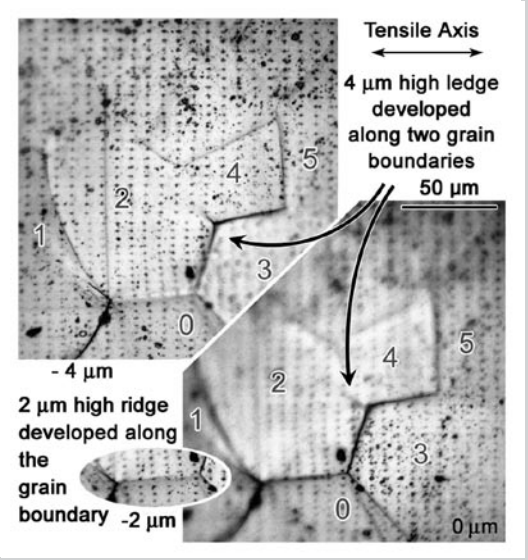

Figure 1. Two images with different focal planes show that vertical displacements of about 4 μm occur along the grain boundaries between grains 2, 3, and 4. In the boundary between grains 0 and 2 (elliptical inset), no ledge developed, but its elevation was higher than the interiors of grains 0 or 2 on either side.

way. These experimental investigations provide an effective environment to evaluate the fidelity of CPFE methods that will help improve their ability to accurately model deformation processes that occur in real microstructures. Strategies to introduce slip transfer processes into grain boundaries that include the capability to monitor residual defect storage are under way. See the sidebar for experimental methods.

OPTICAL MICROSCOPY

A region of a deformed CP Ti specimen bent to about 8% surface tensile strain using 4-point bending is shown in Figure 1. Optical images appear to show grain boundary cracks (curved arrows), but upon closer inspection, these are found to be ledges (with as little as 2% deformation, these ledges can give the appearance of cracks). The ledge geometry is confirmed by changing the focal plane so that different surface features such as dirt or grid marks are in focus. In Figure 1, the elevation of grain 3 is about 4 μm above the neighboring grains in the center. This is shown by comparing the lower micrograph at a focal plane marked 0 μm, and the top micrograph at a focal plane marked –4 μm. Other boundaries do not form ledges, and are not easily seen, such as the one that must lie between grains 2 and 4 in the middle. In some cases, a ridge forms along a boundary between two grains, such as the lower boundary in the elliptical inset at a focal plane of –2 μm that is out of focus at the 0 and –4 μm positions in the other two images. The array of markers clearly shows strain gradients associated with this boundary. This image shows that deformation near grain boundaries can differ significantly from the grain interiors. These features have been further quantified using optical laser profilometry and atomic force microscopy measurements (AFM, or scanning probe microscopy, not shown).

ORIENTATION IMAGING MICROSCOPY

A Schmid factor map made from electronic backscatter pattern (EBSD) data prior to deformation for the area shown in Figure 1 is shown in Figure 2. This region has a mix of hard (black) and soft (white) grains, as prismatic slip has a much lower critical resolved shear stress than basal or other slip systems. After deformation, the grayscale misorientation map in Figure 3 shows the misorientation from a position in the center of the grain (white) up to 10° (black) in the same grain. Along the boundary between grains 2 and 3, and grains 4 and 5, the gradient exceeds 10°. Gradients are often observed in hard grain orientations (those with the c-axis close to the horizontal tensile axis, black in Figure 2), and especially when they are adjacent to neighboring soft grains (e.g., grains 2 and 4 that have their c-axis nearly perpendicular to the horizontal tensile axis). In addition, it is evident that soft grain #4 strained more than other grains, and that the orientation in the grain center changed more than sur-

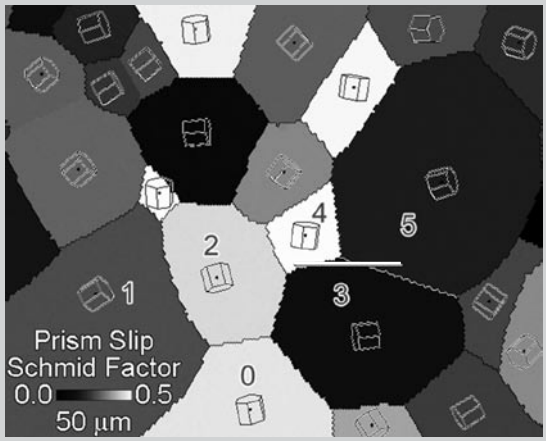

Figure 2. Schmid factor map based upon tension in the horizontal direction of the region in Figure 1; the horizontal line through grains 4, 3, and 5 indicates where 3-D x-ray measurements were made in Figure 4.

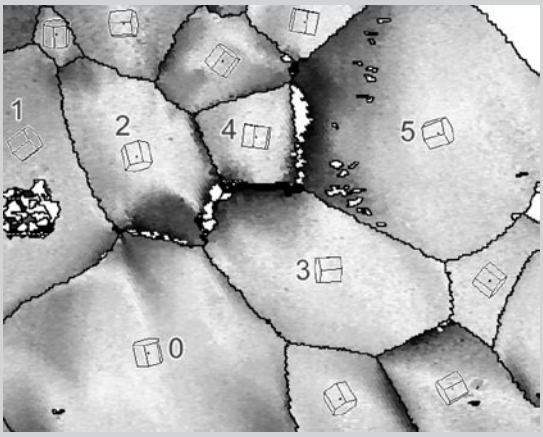

Figure 3. Map of crystal orientation after ~8% tensile strain shows orientation gradients up to 10° (black) from a position in the center of each grain (white), indicated by unit cell orientation. Grains 0 and 4 show the most profound orientation change in the grain interior (from Figure 2).

EXPERIMENTAL METHODS

Well-annealed samples of commercially pure titanium with grain sizes of about 50–200 μm were cut in the shape of 4-point bend specimens with dimensions of 25 × 3 × 2.5 mm and then electropolished. The bending stage was designed so that a strained but still loaded specimen could be investigated in microscopes.[15] An elastic-plastic continuum finite element analysis of this geometry showed that the region between the two middle pins 6 mm apart provided a nearly uniform plastic strain on the surface.[15] Many tools were used to investigate the material before and after deformation: optical microscopy, atomic force microscopy to measure surface topography, differential image correlation using grid marks deposited with a focused ion beam to measure local strains, scanning electron microscopy, transmission electron microscopy, electron backscatter pattern mapping to track grain orientations, orientation gradients and grain boundary misorientations, electron channeling contrast to detect slip activity, and three-dimensional x-ray characterization of local orientations and orientation gradients, boundary inclinations, and internal strains.

rounding grains. Strains measured using the focused ion beam (FIB) deposited markers indicate that hard grains (with the c-axis toward the tensile axis) generally deformed about half as much as soft grains. These strong local orientation gradients suggest that slip transfer across a grain boundary may be difficult to accomplish, as self-accommodation to maintain compatibility with the shape change of a neighboring grain prevents fracture.

3-D X-RAY CHARACTERIZATION

Part of the region illustrated in Figures 1–3 was characterized using microbeam x-ray diffraction analysis capabilities on beamline 34-ID-E at the Advanced Photon Source at Argonne National Laboratory[16,17] to assess subsurface orientation gradients. The white horizontal line in Figure 2 shows the location of a trace on the Schmid factor map where a slice of material was characterized underneath grains 3, 4, and 5 before and after deformation. The undeformed slice

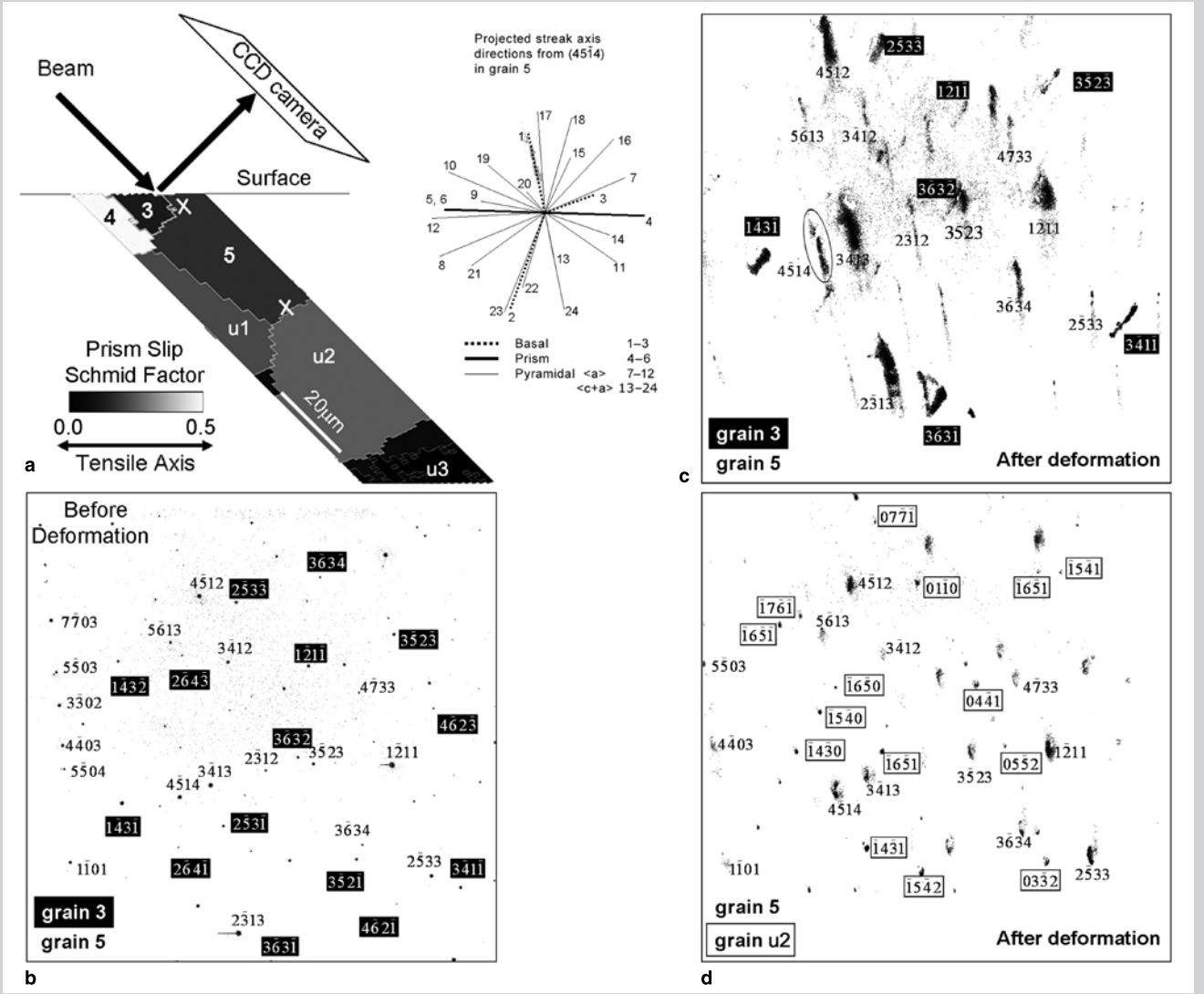

Figure 4. (a) Subsurface crystal orientation map along trace shown in Figure 2 from 3-D x-ray analysis before deformation shows initial grain shape. Diffraction patterns from boundary between grains 3 and 5 near the surface (b) before and (c) after deformation, and diffraction pattern of boundary between grains 5 and u2 about 25 μm below the surface after deformation (d). Between (a) and (c), a spider plot assists identification of dislocations associated with streaked spots in grain 5.

Table I. Schmid Factors for Slip Systems Associated with Streaks on Laue Pattern

Slip System	Global Stress Tensor	Local Stress Tensor (CPFE)
1 (surface)	0.427	0.375
1 (subsurface)	0.364	0.302
24 (surface)	0.027	0.004
24 (subsurface)	0.088	0.110

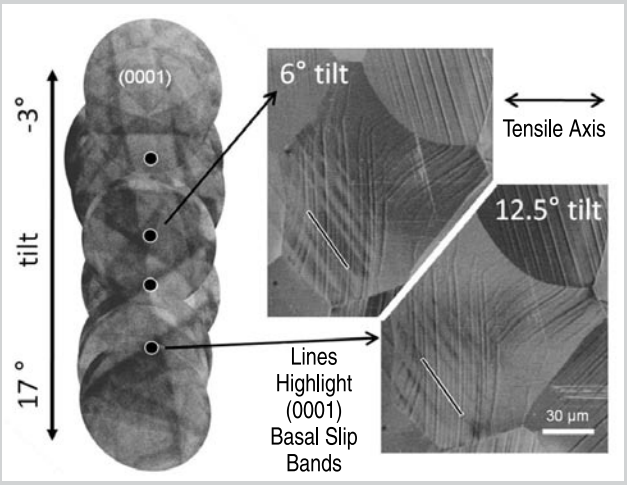

Figure 6. Selected area channeling patterns (SACP) assist in the interpretation of different contrast in images with different sample tilt conditions for the same set of basal slip bands.

is shown in Figure 4a, where the x-ray beam entered the specimen 45° from the surface. There is good agreement between lattice orientations measured by EBSD and by the x-ray method for the surface grains. The x-ray method can identify subsurface grains (U1, U2, and U3), and hence grain boundary inclinations, which result from the high energy beam and the algorithms to reconstruct diffraction patterns from a particular voxel beneath the surface. Figure 4b shows reconstructed and indexed Laue peaks from both grains at the 3–5 grain boundary before deformation. The location of this pattern is marked by the upper left 'X' in Figure 4a. After deformation, Laue reflections of both grains became streaked (Figure 4c), but in different directions, implying that substantial orientation gradients arose from geometrically necessary (unpaired) dislocations (GNDs) present in this small volume. Because the streaking and peak spreading is so pronounced in the deformed grains, it was not possible to automatically identify orientations from the deformed diffraction patterns at all locations in the 3-D scan. However, the streaks can be used to identify slip systems associated with GNDs. Here, we assume that the streaking of a Laue peak of one grain is caused by a single set of edge dislocations, with Burgers vectors **b**, slip plane normal **n**, and dislocation line direction τ (perpendicular to **b** in the slip plane). With this assumption, the streak direction ξ of a certain peak (hkl), which is projected onto the detector, can be written as $\xi = \tau \times \mathbf{g}_{hkl}/|\tau \times \mathbf{g}_{hkl}|$, where $\mathbf{g}_{hkl}$ is the reciprocal lattice vector of the peak.[18,19] Specifically, for the $(4\bar{5}14)$ peak of grain 5, the directions of projected streaks arising from GNDs on each of the 24 dislocation slip systems are plotted (#1–3 for basal, #4–6 for prismatic, #7–12 for pyramidal <*a*> and #13–24 for pyramidal <*c*+*a*>). Comparison between the measured and predicted directions for GND lattice rotation streaks shows that the experimental streak is closest to the prediction for basal slip system 1 or pyramidal <c+a> slip system 24. The streak from the pattern is overlaid on the projected streak axis for basal slip system 1, which has a much higher Schmid factor than the <c+a> system 24 or 13; values for 24 are shown in Table I. However, this analysis does not take into account the fact that the local stress tensor in this grain boundary region differs from the uniaxial tension global stress state. Using the local stress tensor determined from the CPFE model described in the next section, the Schmid factors at this *particular* location are slightly different, but do not alter the interpretation of which slip systems are most likely to be active (but this is not always true). This analysis shows that basal slip is correlated with the observed GNDs.

A similar analysis shows that GNDs in grain 3 are associated with pyramidal <*c*+*a*> slip. The distribution of GNDs is not uniform in most grains. For example, the Laue reflections of grain 5 from a greater depth at the 5-7 grain boundary marked by the lower right 'X' in Figure 4a shows streaking in the same direction as in Figure 4d, but with some differences in shape, which indicates subtle differences in the GND

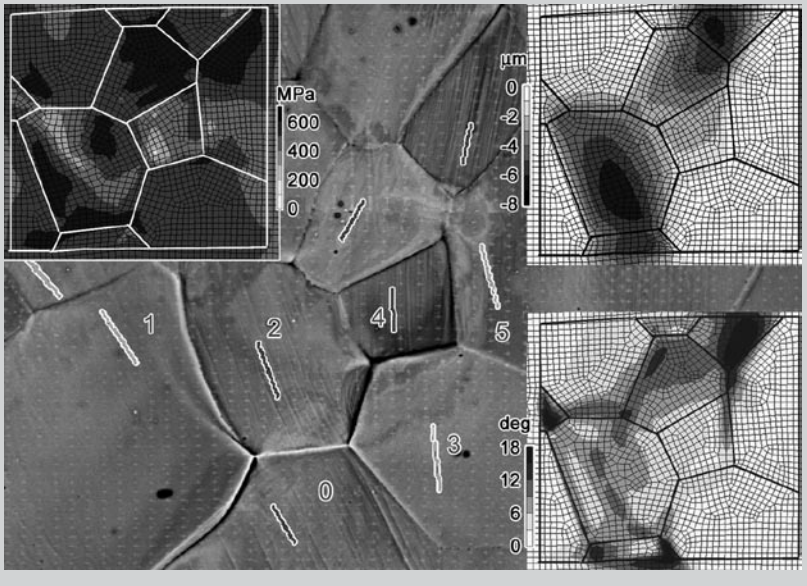

Figure 5. SEM backscattered electron image of microstructure from Figures 1–4 after 8% tensile strain, with CPFE simulation results showing von Mises stress (upper left), surface elevations (upper right), and orientation gradients (lower right). Slip plane traces are indicated for the most highly stressed prism (dark gray) or basal (light gray) slip system based upon the uniaxial tension global stress state.

details. Furthermore, comparing the position of diffraction spots for grain 5 in Figure 4c and d, the lattice orientation at the top and bottom of the grain differs by ~10° in the direction indicated by the streaks.

CRYSTAL PLASTICITY FINITE ELEMENT SIMULATION

A major goal of this research project is to compare experimental measures of strain in patches of microstructure with CPFE simulations of the same microstructure patch. The mesh was extracted from the undeformed geometry in two dimensions, and extended into a five-element thick slab, making the grain boundaries perpendicular to the surface. A rim of elements with the same orientation (similar to the dominant orientation) provided some external constraint to buffer the modeled region from applied boundary conditions. Figure 5 shows a backscattered electron (BSE) image in the same region described above in Figures 1–4. Using the EBSD data, the plane trace for the most highly stressed slip system (based upon the global stress state) are identified in each grain. The CPFE analysis used the fact that the critical resolved shear stress for prismatic slip is 1/3 that for basal slip and 1/4 for <*c*+*a*> slip.[20] Clearly, grains oriented favorably for prismatic slip (dark gray traces) show dramatic slip plane traces and high activity in the CPFE simulation, while evidence for basal slip is not readily observed (lighter gray traces).

The CPFE analysis results are overlaid in the corners of Figure 5. Grains with different orientations behaved quite differently under the simulated applied tensile load. The top left inset in Figure 5 shows the calculated equivalent von Mises stress. Some grains display substantial stress gradients while others do not, and the range of stresses among the grains varies by a factor of 4. The CPFE model also provides the relative z-displacement along the surface normal (upper right inset in Figure 5). The softer grains tended to "sink" into the surface during deformation as they elongated in the tensile direction and contracted normal to the surface. The computed z displacements are mostly comparable in magnitude to the displacements found from the optical microscopy measurements for the grain interiors as well as for the grain boundary regions; the boundary at the bottom of grain 2 is modeled to have sunk by ~5 μm, but was found experimentally to have sunk by ~2 μm, where the ridge was observed in the elliptical inset in Figure 1. However, the sense and location of local grain rotations near grain boundaries was not accurately simulated by the CPFE model (lower right, e.g., top and bottom edges of grain 2 and left side of grain 5). If the deformation patterns near grain boundaries are not modeled correctly, then the deformation in the grain interiors is also affected. Hence, even the modeled deformation patterns in grain interiors also lack credibility. This lack of agreement emphasizes the need to improve the geometrical representation of grains with proper inclinations and orientations beneath the surface, and to install appropriate grain boundary properties into the CPFE modeling strategy.

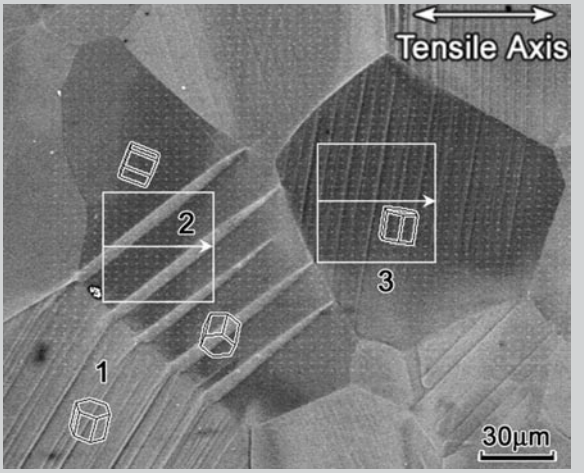

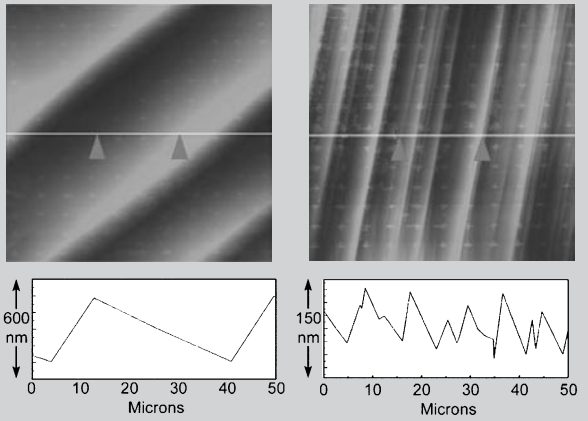

Figure 7. AFM, SEM, and OIM characterization of slip-stimulated twinning from grain 1 to grain 2. AFM measurements provide accurate z displacements that permit quantitative analysis on the active deformation systems in different grains. Prism slip-stimulated twin deformation transfer occurred at the 1–2 grain boundary. No slip-to-twin transfer occurred across the 2–3 boundary.

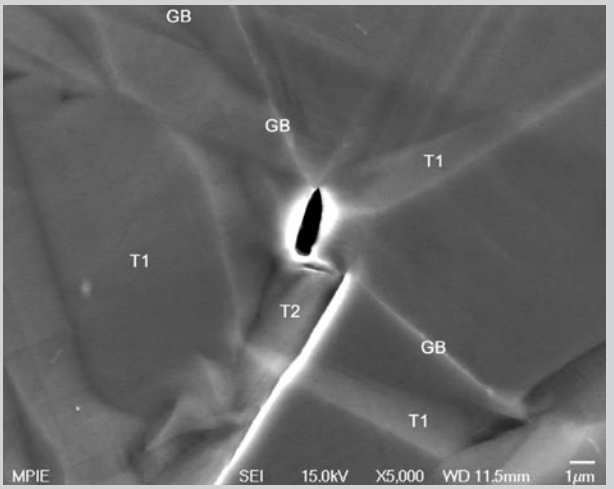

Figure 8. A crack formed at a grain boundary where a $\{1\bar{1}21\} < \bar{1}\bar{1}26 >$ T2 twin interacted with many T1 twins after 2% strain; the T2 twin had a large shear component out of the plane of the page; horizontal tensile axis.

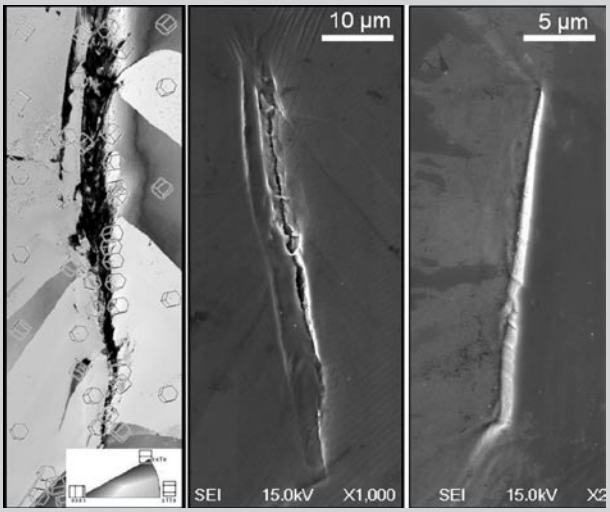

Figure 9. Sample bent to about 15% tensile strain shows GB cracks. The left two show a Mode 1 and the right image shows a Mode II crack.

SCANNING ELECTRON MICROSCOPY

The BSE image in Figure 5 shows significant contrast variations where there are grain orientation gradients and slip traces. These slip traces represent slip bands where the local crystal orientation differs from the majority orientation, and they are in close agreement with computed plane traces for slip systems with high Schmid factors based upon the global stress tensor, as shown by overlaid plane traces. From this and many other observations, it is clear that when prismatic slip is favored, distinct slip bands are observed, which have topographies that are even obvious in secondary electron images. These BSE images show channeling contrast arising from small orientation gradients, both across the breadth of the grains, but also associated with local disruption in channeling conditions due to residual dislocations in the slip bands.[21] When the specimen is more strategically tilted with respect to the beam, as in Figure 6, the channeling conditions change, thus emphasizing particular kinds of defects, in this case basal slip in a particular grain. Consequently, varying the channeling conditions is important to fully identify slip activity that does not cause dramatic topography that is commonly seen with prismatic slip (vertical banding features in Figure 6). At low magnification, the (0001) basal plane slip bands highlighted by the overlaid plane trace lines shows opposite contrast when the sample was tilted from 6 to 12.5°, such that the beam axis was on one side or the other side of a diffraction channeling band.

SCANNING PROBE MICROSCOPY

To provide detailed experimental evidence that assists and guides the development of CPFE simulation of twinning and dislocation interactions, a combination of AFM, BSE imaging, and EBSD was performed, allowing quantitative analysis of the active deformation systems in different grains (an example is given in Figure 7). The surface height change (h) due to the dislocation and/or twinning activity can be measured from the AFM data, while orientation imaging microscopy (OIM) and scanning electron microscopy (SEM)-based trace analysis allows the deformation plane to be identified. Taken together, this information enables the Burgers vector directions to be determined. Thus, the number of slip/twinning dislocations shearing a given volume of material can be calculated as $h = Nb \cdot n_{surface}$, where N is the number of dislocations, b is the magnitude of the Burgers vector, and $n_{surface}$ is the normal to the slip plane. Because only one twinning partial moves on each adjacent slip plane during the formation of a twin (unlike dislocation slip, where many dislocations may move on a given plane), twins can be used to check the accuracy of this measurement strategy by comparing the projected twin width measured from BSE images to the calculated projected twin width based on the inter-planar spacing and the number of twinning dislocations determined from AFM. For the largest twin shown in Figure 7, the calculated apparent width is about 5.2 µm, which is quite close to the measured width of 5.6 µm. Similar analysis can be used on a series of parallel slip bands in a grain, such as the slip bands shown in Figure 7. This approach is allowing us to measure the local shear strains on particular deformation systems throughout a microstructure patch for direct comparison with calculated shears from the CPFE model. Local deformation gradients and strains can be quantified in detail with local displacement information via digital image correlation (DIC) using markers placed on selected regions (evident in Figures 1 and 5), and compared with the contribution of shears on particular slip systems.

This effort has also uncovered a subtle 180° rotation about the normal direction of the coordinate system for the Euler angles with respect to the physical specimen (map) coordinate system. For most analyses, this ambiguity has no impact, but when the sense of 3-D shears is important, this difference in coordinate systems must be considered. Correcting the Euler angles led to significant improvements in agreement between the CPFE simulation and experimental measurements. Researchers should take care to ensure that their systems produce orientation data in the expected sense in similar types of analyses. Updated details regarding coordinate systems are discussed extensively in Reference 22.

MECHANICAL TWINS AND DAMAGE NUCLEATION

While twinning is known to be an important deformation mechanism in titanium, the nature of twin nucleation and the role twinning plays in damage nucleation is not known. Figure 7 shows an example of nucleation of $\{10\bar{1}2\}<\bar{1}011>$ (type T1 tensile/extension) twins in grain 2 at the intersection of prismatic dislocation slip bands in grain 1 with the grain boundary. Based on this and similar observations, we have found a statistically significant correlation between the prismatic dislocation slip in soft oriented grains and nucleation of twins in hard oriented grains. Specifically, if the alignment of the slip and twinning systems is

quantified by a slip transfer parameter m' = cosψ cosκ, where ψ is the angle between the slip and twinning plane normals and κ is the angle between the slip and twinning directions,[23] the correlation between prismatic slip and T1 twinning in neighboring grains is high for large values of m'. Non-parametric statistical analysis reveals this correlation is much stronger than for other variables, such as the Schmid factors of the slip and twinning systems.[24]

Furthermore, preliminary results suggest that twinning plays an important role in nucleating damage in Ti. While $\{11\bar{2}1\}<\bar{1}\bar{1}26>$ (type T2 tensile/extension) twinning is quite rare in our studies, formation of T2 twins does appear to result from deformation transfer associated with T1 twins interacting with boundaries. Furthermore, we have observed the formation of severe ledges and one crack in association with T2 twinning. Figure 8 shows a nucleated crack developing along the interfacial plane of a T2 twin where it intersects at a grain boundary after only 2% strain. The actual reason these cracks formed is not yet understood, but this T2 twin has a large out-of-plane shear component. The cracking may either be the result of the large shear strain ($\gamma = 0.630$ for T2 twins as compared with 0.175 for T1 twins), or from subsequent plastic deformation incompatibility at the twin boundary after the twin formation.

Two kinds of cracks have been observed at strains of ~15%. Figure 9 shows the development of an intergranular crack after a strain of ~15%. Intense T1 twin activity occurred on both sides of the original grain boundary, apparently resulting in incompatible shears at the boundary. In a nearby region, a large grain boundary ledge developed (right side of Figure 9), where an abrupt ledge along the grain boundary suggests that either grain boundary sliding or mode II cracking occurred. Further analysis of these twins will be the subject of future papers.

EVOLVING MEASURES OF DAMAGE NUCLEATION CRITERIA

Our prior work on TiAl led to the identification of a fracture initiation parameter associated with local twin strains in grain boundary regions.[25–27] This fracture initiation parameter was experimentally developed as a static measure based upon initial grain orientations, to quantitatively assess imperfect slip transfer across grain boundaries. This parameter, which distinguishes between cracked and intact boundaries, is simply the product of three terms: the Schmid factor of the most highly stressed twinning system, m_{tw}, the scalar product of the twin Burgers vector direction and the maximum tensile stress direction, $\mathbf{b}_{tw} \cdot \mathbf{t}$, and a sum of scalar products between the same highly stressed Burgers vector and possible accommodating ordinary dislocation directions in the adjacent grain, i.e. $fip = m_{tw} \left| \mathbf{b}_{tw} \cdot \mathbf{t} \right| \Sigma \left| \mathbf{b}_{tw} \cdot \mathbf{b}_{ord} \right|$, where all vectors are of unit length.

The *fip* is large when imperfect slip transfer is maximized. Recent work has generalized the *fip* to use information that is readily available in CPFE computations so that the m_{tw}, $\mathbf{b}_{tw}$, $\mathbf{b}_{ord}$, and $\mathbf{t}$ are evaluated on a local mesoscale basis.[28] This allows for the evolving and spatially heterogeneous lattice shears to be incorporated directly into the calculation of an *evolutionary fip* that varies over time and space. Figure 10 shows the first two parts of the *fip* evaluated at three time steps in the boundary between grains 14 and 15, which exhibited microcracks, and at the boundaries of grains 14 and 17 or 13 and 16, which did not develop microcracks. The *fip* values evolved in all three boundaries, but it was the highest in the boundary that cracked. This kind of modeling has not yet been developed for CP Ti, as the deformation

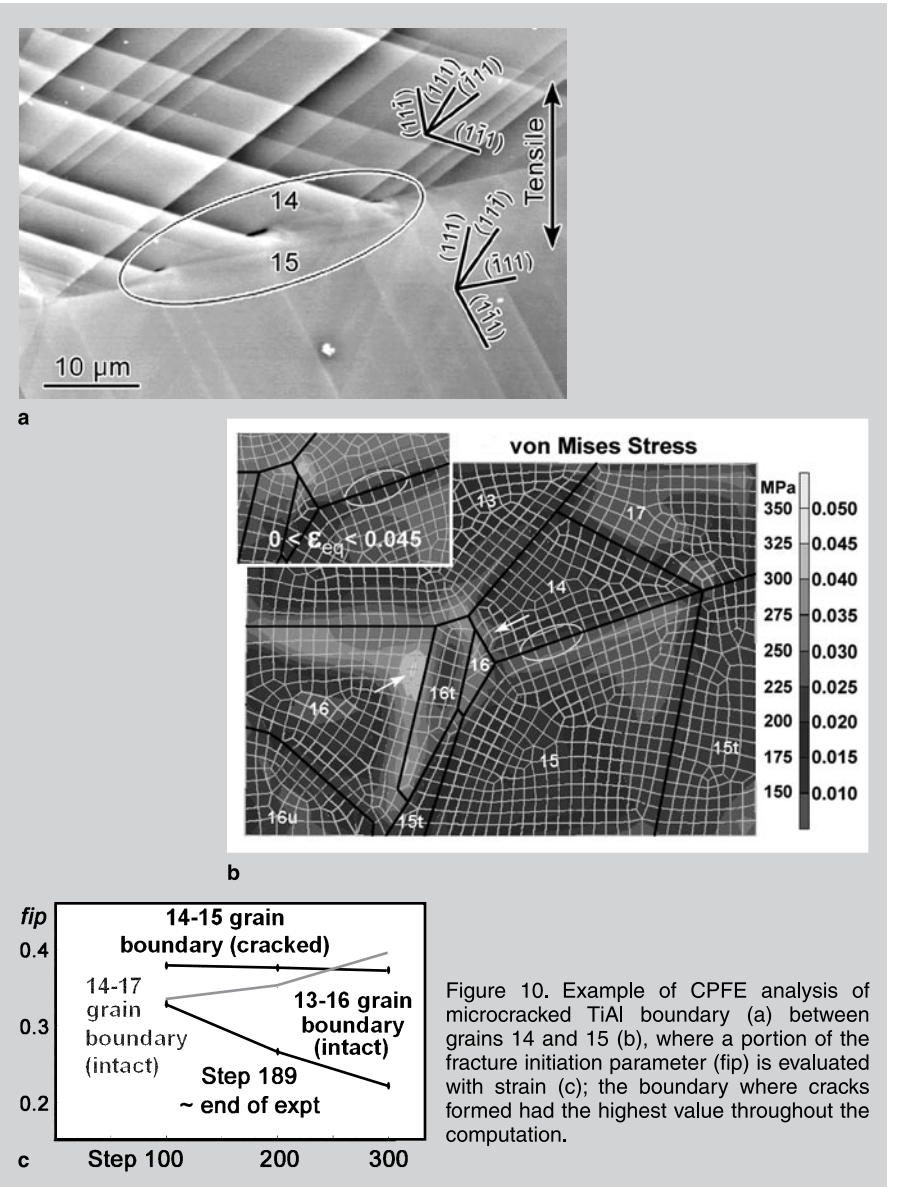

Figure 10. Example of CPFE analysis of microcracked TiAl boundary (a) between grains 14 and 15 (b), where a portion of the fracture initiation parameter (fip) is evaluated with strain (c); the boundary where cracks formed had the highest value throughout the computation.

transfer processes at grain boundaries are still being investigated.

CONCLUSIONS

Correlated experimental and computational studies of the details of slip transfer between grains are under way, and insights about the relationship between heterogeneous deformation, mechanical twinning, and damage nucleation are developing. In both CP Ti and TiAl, twins that exhibit large shear strains are correlated with microcrack nucleation in some boundaries. In TiAl, a relatively simple fracture initiation parameter has been identified that can identify which boundaries are more likely to crack when mechanical twins interact with the boundary. The greater complexity of deformation in CP Ti, with more types of active twinning systems, and the inherently larger ductility implies that a fracture initiation parameter will need to be more sensitive to heterogeneous strain evolution than is needed for predicting crack nucleation in TiAl.

ACKNOWLEDGEMENTS

This research is supported by a Materials World Network grant (NSF DMR-0710570 and DFG EI 681/2-1). The TiAl work was supported by the Air Force Office of Scientific Research contract # F49620-01-1-0116, and by the Michigan State University Composite Materials and Structures Center. Use of the Advanced Photon Source was supported by the U.S. Department of Energy, Office of Science, Office of Basic Energy Sciences, under Contract No. DE-AC02-06CH11357. We thank R. Barabash for helpful insights.

References

1. R.A. Lebensohn and C.N. Tome, *Acta Metall. Mater.,* 41 (9) (1993), pp. 2611–2624.
2. I. Karaman et al., *Acta Mater.,* 48 (9) (2000), pp. 2031–2047.
3. Z. Yao and R.H. Wagoner, *Acta Metall. Mater.,* 41 (2) (1993), pp. 451–468.
4. F. Delaire, J.L. Raphanel, and C. Rey, *Acta Mater.,* 48 (5) (2000), pp. 1075–1087.
5. D. Raabe et al., *Acta Metall. Mater.,* 49 (2001), pp. 3433–3441.
6. P.R. Dawson, D.P. Mika, and N.R. Barton, *Scripta Mater.,* 47 (10) (2002), pp. 713–717.
7. J.D. Clayton and D.L. McDowell, *Mech. Mater.,* 36 (9) (2004), pp. 799–847.
8. S. Hao et al., *Comput. Methods Appl. Mech. Engrg.,* 193 (2004), pp. 1865–1908.
9. A. Ma, F. Roters, and D. Raabe, *Acta Materialia,* 54 (8) (2006), pp. 2181–2194.
10. K.S. Cheong and E.P. Bussso, *J. Mechanics Physics Solids,* 54 (2006), pp. 671–689.
11. J.A. Querin, J.A. Schneider, and M.F. Horstemeyer, *Materials Science and Engineering A,* 463 (1-2) (2007), pp. 101–106.
12. T.R. Bieler, P.D. Nicolaou, and S.L. Semiatin, *Metallurgical and Materials Transactions A,* 36A (1) (2005), pp. 129–140.
13. T.R. Bieler, R.L. Goetz, and S.L. Semiatin, *Mater. Sci. Eng.,* A405 (2005), pp. 201–213.
14. S. Ankem et al., *Progress in Materials Science,* 51 (2006), pp. 632–709.
15. B. Wagenknecht, D. Libiran, S. Poon, and K. Sztykiel, "In-situ Four-Point Bending Apparatus for Scanning Electron Microscopes" (Senior Design Project, Mechanical Engineering, Michigan State University, April 2008).
16. B.C. Larson et al., *Nature,* 415 (2002), pp. 887–890.
17. W. Liu et al., *Ultramicroscopy,* 103 (2005), pp. 199–204.
18. R.I. Barabash et al., *Applied Physics Letters,* 79 (2001), pp. 749–751.
19. R.I. Barabash, G.E. Ice, and F.J. Walker, *J. Applied Physics,* 93 (2003), pp. 1457–1464.
20. X. Wu et al., *Acta Materialia,* 55 (2007), pp. 423–432.
21. M.A. Crimp, *Microscopy Research and Technique,* 69 (2006), pp. 374–381.
22. B. El-Dasher et al., Analysis of EBSD Data (L17), retrieved from ftp site *neon.materials.cmu.edu/rollett/27750/27750.html* (2009).
23. J. Luster and M.A. Morris, *Metall. Mater. Trans. A,* 26 (1995), p. 1745.
24. L. Wang et al., *Metall. Mater. Trans.,* in press.
25. B.A. Simkin, M.A. Crimp, and T.R. Bieler, *Scripta Materialia,* 49 (2) (2003), pp. 149–154.
26. T.R. Bieler et al., *J. Engineering and Materials Technology,* 130 (2008), 021012.
27. T.R. Bieler et al., *International Journal of Plasticity,* 25 (2009), pp. 1655–1683.
28. D.E. Mason, unpublished research (2009).

T.R. Bieler, M.A. Crimp, Y. Yang, and L. Wang are with the Department of Chemical Engineering and Materials Science, Michigan State University, East Lansing, MI 48824; P. Eisenlohr is with Max-Planck-Institut für Eisenforschung, Düsseldorf, Germany; D.E. Mason is with Albion College, Albion, MI; W. Liu is with Advanced Photon Source at Argonne National Laboratory, Argonne, IL; and G.E. Ice is with Oak Ridge National Laboratory, Oak Ridge, TN. Prof. Bieler can be reached at bieler@egr.msu.edu.